Computers and Structures 254 (2021) 106580

Contents lists available at ScienceDirect

Computers and Structures

journal homepage: www.elsevier.com/locate/compstruc

Effective elastic and fracture properties of regular and irregular masonry from nonlinear homogenization

Tomáš Krejčí [a], Tomáš Koudelka [a], Vasco Bernardo [b], Michal Šejnoha [a,*]

[a] Department of Mechanics, Faculty of Civil Engineering, Czech Technical University in Prague, Thákurova 7, 166 29 Prague 6, Czech Republic
[b] National Laboratory of Civil Engineering, Avenida do Brasil, 101, 1700-066 Lisboa, Portugal

ARTICLE INFO

Article history:
Received 9 January 2021
Accepted 13 May 2021
Available online 4 June 2021

Keywords:
Regular masonry
Irregular masonry
Damage
Homogenization
Mixed boundary conditions

ABSTRACT

Prediction of effective elastic and strength parameters of both regular and irregular masonry walls from homogenization is presented. To that end, the widely accepted first order homogenization method is adopted to provide the homogenized elastic stiffnesses or compliances as well as macroscopic parameters of the selected nonlinear constitutive models. These include the tensile and compressive strength and fracture energies of a generally orthotropic material extracted from the computationally derived macroscopic stress strain curves. In this regard, two types of boundary/loading conditions resulting from the strain-based and mix type formulation of the homogenization problem are examined. The response provided by an orthotropic damage model, expected to describe the behavior of the homogenized structure on macroscale, is compared to that derived via a classical isotropic scalar damage model. It reveals that strong constraints of the orthotropic damage model offer results inapplicable for estimating the macroscopic fracture properties thus promoting the application of a simple isotropic damage model when solving the homogenization problem. The results also show that the mixed boundary conditions, allowing us to represent a pure tension/compression loading mode while being capable of tracking the softening branch of the stress–strain curve, deliver the response comparable to that of a purely strain-based formulation.

1. Introduction

Numerical homogenization is adopted here to address the macroscopic response of a regular as well as an irregular masonry. The literature offers a voluminous list of contributions devoted to this subject spreading from a complex fully coupled multiscale analysis [1–4] to more engineering friendly approaches decoupling the meso and macro analyses. Therein, the macroscopic analysis builds upon the application of effective properties derived from an independent computational homogenization step performed on a suitable representative volume element (RVE) on mesoscale [5–7]. This latter cathegory of modeling strategies includes also an important group of works utilizing the concept of limit state analysis [8–11], which, when combined with computational homogenization at an RVE level, allows us to estime the macroscopic strength enevelopes [12–16] playing the role of initial failure surfaces on macroscale. The present contribution proceeds along the same lines. To get a broader insight into various modeling strategies of masonry structures the interested reader may consult a comprehensive review of this subject given in [17].

Proceeding in the footsteps of [5] we wish to address a potential applicability of homogenization to feed a suitable macroscopic constitutive model capable of reflecting the intrinsic material anisotropy. To that end, a simple modification to an anisotropic damage model originally introduced in [18] is proposed. Derivation of the required model parameters from homogenization is, therefore, the primary focus. Given the model formulation, we limit our attention to tensile failure of a masonry panel subjected to inplane loading. Such an analysis has typically been confined to a standard strain-based formulation. To advance from a uniaxial strain response to that of a uniaxial stress yet being able to follow the softening branch of the stress–strain curve, the mixed loading/boundary conditions are adopted. In preparation for a full scale analysis of large masonry structures, the predictions provided by the anisotropic damage model, here exploited in its original format, are compared to that of a simple isotropic scalar damage model promoted, e.g., in [5].

The issue of general applicability of the mentioned computational framework is tested on two examples of masonry mesostructures. The first example represents a family of regular

* Corresponding author.
E-mail addresses: krejci@fsv.cvut.cz (T. Krejčí), tomas.koudelka@fsv.cvut.cz (T. Koudelka), vbernardo@lnec.pt (V. Bernardo), sejnom@fsv.cvut.cz (M. Šejnoha).

https://doi.org/10.1016/j.compstruc.2021.106580
0045-7949/

Nomenclature

ω	Scalar damage parameter, [–]
D^t_α	Damage parameter in tension in principal direction α, [–]
D^c_α	Damage parameter in compression in principal direction α, [–]
f_t	Tensile strength, [Pa]
f_c	Compressive strength, [Pa]
w_{cr}	Crack opening displacement, [m]
w_{cr0}	Parameter controlling slope of softening branch [m]
l_{ch}	Element characteristic length, [m]
κ	Mazars' equivaent strain, [–]
$\boldsymbol{\sigma}$	Stress vector, [Pa]
$\boldsymbol{\varepsilon}$	Strain vector, [–]
$\mathbf{L}$	Elastic stiffness matrix, [Pa]
$\mathbf{M}$	Elastic compliance matrix, $\left[\mathrm{Pa}^{-1}\right]$
L	Instantaneous (secant) stiffness matrix, [Pa]
E_i	Young's modulus in material orthotropy direction i, [Pa]
G_{ij}	Shear modulus, [Pa]
ν_{ij}	Poisson's number, [–]
X^{hom}	Homogenized quantity
$\boldsymbol{\Sigma}$	Macrocscopic stress vector, [Pa]
$\boldsymbol{E}$	Macroscopic strain vector, [–]
$\boldsymbol{\varepsilon}^*$	Fluctuation strain, [–]
Ω	Periodic unit cell domain, $[\mathrm{m}^3]$
c_r	Volume fraction of phase r, [–]
L	RVE length, [m]
H	RVE height, [m]
L_{cr}	Total length of traction free surfaces, [m]
A_{cr}	Area of fracture surface, $[\mathrm{m}^2]$
a	Notch size, [m]
G_f	Average fracture energy, $\left[\mathrm{Nm}^{-1}\right]$
G_F	Size independent fracture energy, $\left[\mathrm{Nm}^{-1}\right]$

Abbreviations

RVE	Representative volume element
PUC	Periodic unit cell
ODM	Orthotropic damage model
SDM	Isotropic scalar damage model

masonry with a periodic arrangement of bricks, while the second example shifts attention towards an irregular or random masonry typical of historical structures.

To demonstrate the behavior of a regular masonry panel we ground on our initiative study on Placa masonry presented in [19,20]. Although the origin of Placa buildings dates back to the period of 1930–1960 [21], they represent more than 30% of the Portuguese housing stock [22]. These buildings are often located in the areas with a moderate to high seismic risk. This explains a considerable interest in the determination of their bearing capacity as they show high vulnerability to damage when subjected to seismic loads mainly because of insufficient strength and deformation capacity of masonry walls. This can be put in the context with the fact that no impact of earthquake has been considered in their design, see Fig. 1(c), as the first Portuguese seismic design regulation appeared not until 1958. The figure shows a variety of masonry arrangements ranging from a quarry masonry in exterior walls and foundation to a regular masonry used for interior walls, the latter being the subject of our investigation.

To examine the class of an irregular masonry we turn our attention to the group of historical churches located in the Broumov region in the Czech Republic. For illustration, we present in Fig. 2 (c) the Church of All Saints built in the period of 1722–1723 in accordance with the project of Kilian Ignaz Dientzenhofer.

The Broumov territory often experiences unpleasant climatic conditions with heavy rains and cold weather, which, together with the lack of knowledge of the quality of subsoil at the time of construction, led to the design unable to prevent a differential settlement and consequently the evolution of progressive damage. See, e.g., [23] for invitation to this subject. The need for introducing some rehabilitation measures goes hand in hand with the prediction of the current state of damage and its cause.

Herein, we enter this subject by estimating the pre- and post-peak behavior of several masonry panels similar to those plotted in Figs. 2(a,b). Because deriving a single representative volume element reflecting a random nature of the masonry over a large volume of the church goes beyond the present scope, we consider several test windows of variable size just to demonstrate the importance of the concept of so called statistically equivalent periodic unit cell if we wish to address random microstructures properly, see [24,6,25,12, to name a few]. Another simplification accepted in numerical simulations concerns the material variability evident in Fig. 2. Although mostly sandstones appear in the outer-leaf of the masonry wall, their material properties may vary considerably given their different geological origin. However, in the present study, a two-phase material system is considered adopting the material properties pertinent to that of the highest volume fraction. While this may influence the predicted homogenized elastic properties, it will have only a minor impact on the observed failure mechanism governed merely by mesostructural details and material properties of the mortar phase.

The paper is organized as follows. Following this introductory part, we proceed in Section 2 with a brief review of the two constitutive models. The basic principles of first-order homogenization, covering also the difference between the strain-based formulation and mixed type of loading/boundary conditions, are summarized next in Section 3. The core of the paper devoted to individual simulation scenarios is described in Section 4. The essential findings are presented in Section 5.

2. Constitutive model and material properties

Given its composition, masonry is generally quantified as a quasi-brittle material. It is strong in compression, relatively week in tension, and exhibits a strong strain-softening when exceeding the strength limits. Evolution of tensile cracks makes this material discontinuous. The failure process is typically accompanied by elastic stiffness degradation manifested by evolution of plastic strains.

Such a complex behavior is difficult to simulate numerically leading to simplifying assumptions. Expecting the dominant failure mode be the tensile cracking we rely on standard damage models in describing the masonry response. Although observed experimentally, e.g., in the case of cyclic loading, we do not attempt to address the evolution of permanent strains by coupling damage with plasticity [26,27]. Instead, we focus on comparing the prediction of macroscopic response by simple isotropic scalar damage model [28] and more advanced orthotropic damage model [18], which appears as a suitable candidate for the modeling of homogenized masonry on the structural scale. Although well known, we

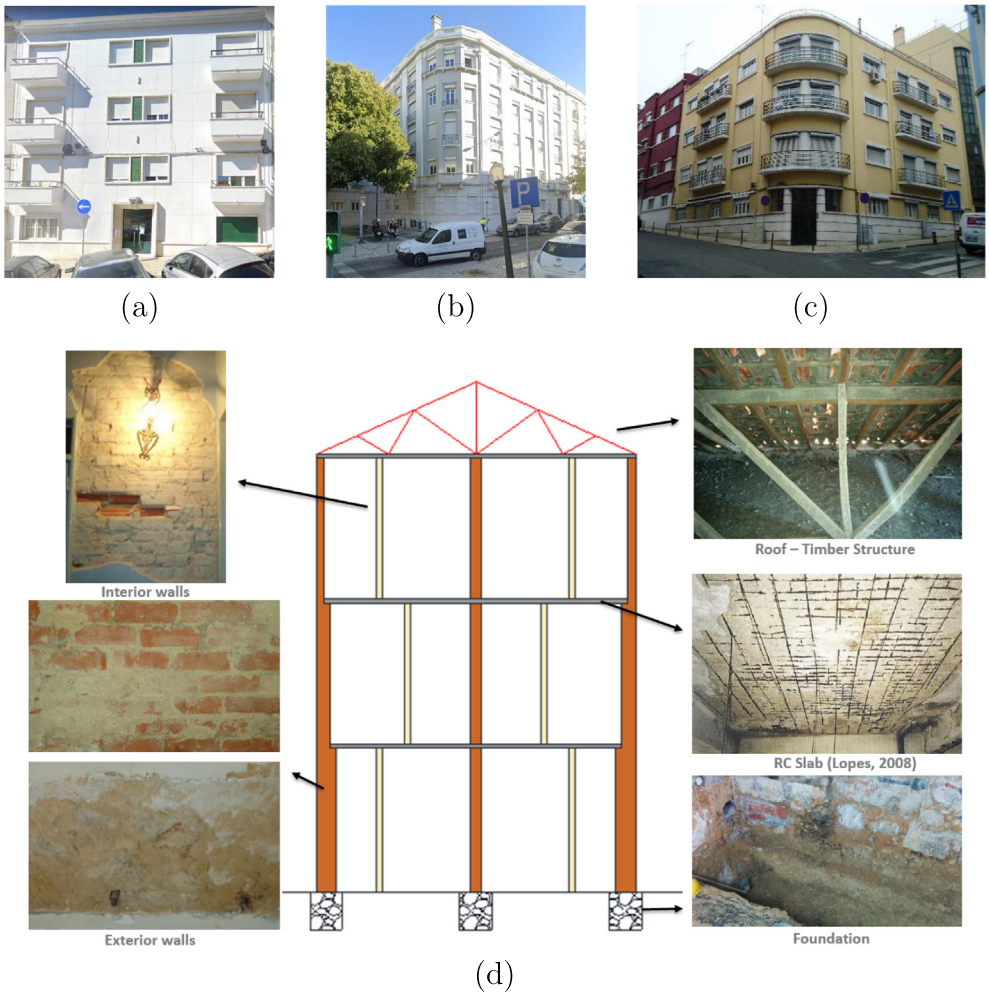

Fig. 1. (a)-(c) Examples of Placa buildings, (c) Scheme of Placa building typology with various types of masonry walls.

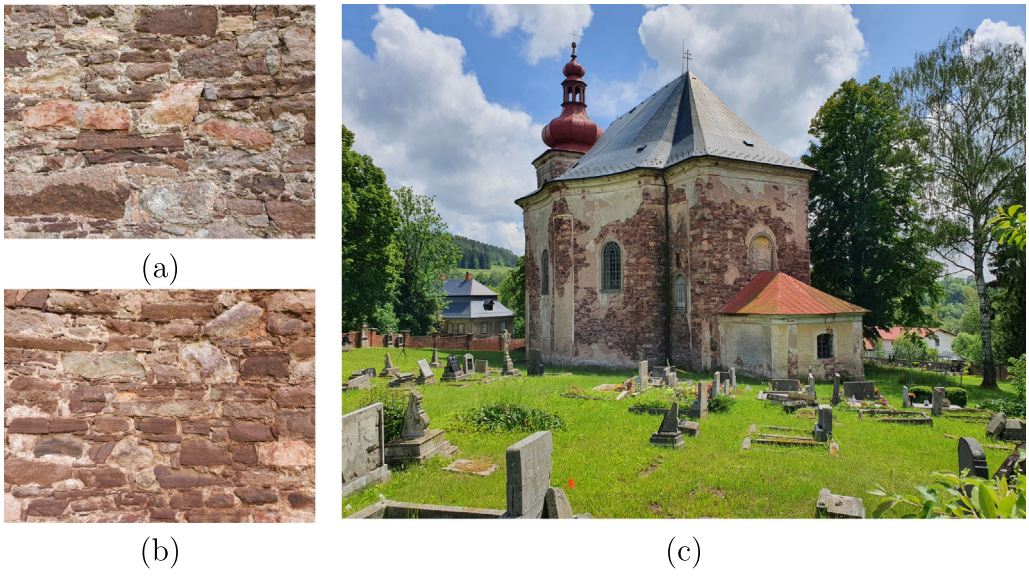

Fig. 2. (a)-(b) Examples of irregular masonry panels, (d) Church of All Saints, Heřmánkovice, Broumov.

present a short exposition to both models for the sake of completeness. Both models were implemented into an in-house finite element program SIFEL [29] used in all presented simulations.

2.1. Isotropic scalar damage model

In the most simple case of a scalar isotropic damage model, the damage evolution is governed by a dimensionless damage parameter ω written for a one-dimensional case as

$$\omega = \frac{A_d}{A}, \tag{1}$$

where A_d is the part of the cross section with evolved defects, i.e. with the material in a damaged state, and A is the total cross section area. The corresponding stress–strain relation reads

$$\boldsymbol{\sigma} = (1-\omega)\mathbf{L}\boldsymbol{\varepsilon} = L\boldsymbol{\varepsilon}, \tag{2}$$

where $\boldsymbol{\sigma}$ and $\boldsymbol{\varepsilon}$ are the stress and strain vectors, $\mathbf{L}$ is the elastic stiffness matrix, and L is the instantaneous (secant) stiffness matrix. The scalar damage parameter $\omega \in [0;1]$ characterizes the material state. The transition states from virgin state $\omega = 0$ to the state of fully evolved defects $\omega = 1$ are described by the damage evolution law.

We adopt one-dimensional traction separation law given by [28]

$$\sigma = f_t \exp\left(-\frac{w_{cr}}{w_{cr0}}\right), \tag{3}$$

where f_t is the tensile strength, w_{cr} is the crack opening and w_{cr0} is the parameter controlling the slope of the softening branch, see Fig. 3. The one-dimensional format of Eq. (2) reads

$$\sigma = (1-\omega)E\varepsilon = E(\varepsilon - \omega\varepsilon) = E(\varepsilon - \varepsilon_d), \tag{4}$$

where E is the Young's modulus of the corresponding isotropic material and $\varepsilon_d = \omega\varepsilon$ is the strain component attributed to the attained damage. To partially avoid mesh dependency of the results typical of materials with softening the crack opening is smeared over the element as [28]

$$\varepsilon_d = \omega\varepsilon = \frac{w_{cr}}{l_{ch}}, \tag{5}$$

where l_{ch} is the element characteristic length. For complex multidimensional stress/strain states, the strain ε may be substituted by the Mazars equivalent strain κ provided by [30]

$$\kappa = \sqrt{\sum_{\alpha=1}^{3} \langle \varepsilon_\alpha \rangle_+^2}, \tag{6}$$

where $\langle\cdot\rangle_+$ stands for the positive component. Combining Eq. (4) with Eqs. (5) and (3) and replacing the strain ε with the maximum equivalent strain in the loading history $\bar{\kappa}$ yields the resulting nonlinear equation

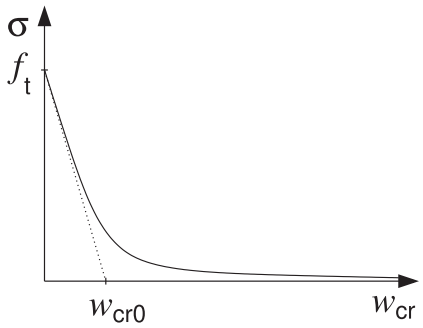

Fig. 3. One-dimensional traction separation law.

$$(1-\omega)E\bar{\kappa} = f_t \exp\left(-\frac{\omega l_{ch}\bar{\kappa}}{w_{cr0}}\right), \tag{7}$$

to be solved for the damage parametr ω for states where $\bar{\kappa}$ exceeds the elastic threshold $\varepsilon_0 = f_t/E$.

2.2. Orthotropic damage model

While the scalar isotropic damage model can be used successfully for the description of 1D stress states, e.g., 1D tension or bending, it may become impractical for multi-dimensional stress states and generally anisotropic materials, because it reduces all components of $\mathbf{L}$ to zero even in cases when damage evolves in one direction only, recall Eq. (2). A suitable modification was proposed in [18] leading to an anisotropic damage model.

The authors still assume an isotropic material but allow for an independent evolution of damage in three-perpendicular directions in strain-space. By introducing two independent damage parameters D_α^t and D_α^c for tension and compression, respectively, they provide an equivalent format of Eq. (7) in the form [32]

$$\left(1 - D_\alpha^\beta\right) E|\bar{\varepsilon}_\alpha^\beta| = f_\beta \exp\left(-\frac{D_\alpha^\beta l_{ch}|\bar{\varepsilon}_\alpha^\beta|}{w_{cr0}^\beta}\right), \tag{8}$$

where $\beta \in [t,c]$ identifies either tensile or compressive failure, α represents the principal strain direction, and $\bar{\varepsilon}_\alpha^\beta$ is the maximum principal strain in the loading history, equivalent to $\bar{\kappa}$ in Eq. (7). Further details regarding practical applications of both models can be found in [31,32].

The present formulation can be advanced beyond material isotropy at the structural level through the following adjustments. First write the stress–strain law in terms of principal stresses σ_α and strains ε_α as

$$\sigma_\alpha = \left(1 - H(\varepsilon_\alpha)D_\alpha^{(t)} - H(-\varepsilon_\alpha)D_\alpha^{(c)}\right)\overline{\sigma}_\alpha, \quad \overline{\boldsymbol{\sigma}} = \mathbf{L}^{\mathrm{hom}}\boldsymbol{\varepsilon}, \tag{9}$$

where H denotes the Heaviside function, $\overline{\sigma}_\alpha$ stands for the effective stress, and $\mathbf{L}^{\mathrm{hom}}$ represents the homogenized elastic stiffness matrix, see ahead Section 3. The traction separation law (10) is now written as

$$\left(1 - D_\alpha^{(\beta)}\right) L_{\alpha\alpha}^{\mathrm{hom}}|\bar{\varepsilon}_\alpha^{(\beta)}| = f_\alpha^{(\beta)} \exp\left(-\frac{D_\alpha^{(\beta)} l_{ch}|\bar{\varepsilon}_\alpha^{(\beta)}|}{w_{cr0,\alpha}^{(\beta)}}\right), \tag{10}$$

where $L_{\alpha\alpha}^{\mathrm{hom}}$ are the diagonal components of $\mathbf{L}^{\mathrm{hom}}$. Applicability of Eq. (10) is now tested by modeling the response of church in Fig. 2(c) to differential settlement and annual change of temperature being the principal sources of damage of the Broumov group of churches.

2.3. Material properties of masonry constituents

The basic material parameters needed in both damage models are stored in Table 1. They were found from a series of laboratory measurements performed on samples extracted from existing structures.

The Placa masonry consists of clay bricks and mortar produced from the cement, lime, and sand mixture in the proportions of 1:3. To collect the required properties, the specimens extracted during rehabilitation works from a building located in the center of Lisbon were examined in the National Laboratory for Civil Engineering in Portugal (LNEC). Further details on the actual experimental program are available in [33–35].

Experimental investigation of the properties of stones used in the construction of outer walls of Broumov churches combined both nondestructive on site tests using the Schmidt hammer and standard laboratory compression tests on cylindrical samples drilled from various stones. The results are available in [36] with

Table 1
Material parameters of mortar, brick (Placa) and sandstone (Broumov).

Material	Parameter		Placa	Broumov
Mortar	E	[GPa]	0.7	0.13
	ν	[–]	0.2	0.17
	f_c	[MPa]	1.3	1.5
	f_t	[MPa]	0.1	0.1
	w_{cr0}	[m]	10^{-4}	10^{-4}
	G_F	[N/m]	10	10
Brick or Sandstone	E	[GPa]	13.0	20
	ν	[–]	0.2	0.2
	f_c	[MPa]	40	45
	f_t	[MPa]	2	2.25
	w_{cr0}	[m]	2.9×10^{-5}	2.9×10^{-5}
	G_F	[N/m]	58	65.25

the compressive strength f_c of sandstone ranging from 40 to 50 MPa. Because of a two-phase material system assumed in our numerical analysis, the value of $f_c = 45$ MPa was adopted. However, it will be seen that the fracture properties of stones play no role owing to a weak mortar. The tensile strength f_t was estimated as 1/20 of f_c. The fracture energy in tension was set to $G_F = df_t$ with the ductility index $d = 0.029$ mm [37]. The material properties of mortar were taken from [38]. For the adopted exponential softening law, we get $w_{cr0} = G_F/f_t$, which follows from the definition of fracture energy as the area under the traction separation diagram in Fig. 3. The relations for G_F and w_{cr0} were used also for the Placa masonry.

3. Homogenization and effective elastic properties

Consider a two-phase material system loaded on its outer boundary by the selected components of the prescribed surface displacements and tractions that would generate macroscopic uniform strains $\boldsymbol{E}$ and stresses $\boldsymbol{\Sigma}$ in an equivalent homogeneous medium. Such loading conditions allow us to invoke the Hill lemma [39]

$$\langle \delta\boldsymbol{\varepsilon}^{\mathrm{T}}(\boldsymbol{x})\Delta\boldsymbol{\sigma}(\boldsymbol{x})\rangle = \delta\boldsymbol{E}^{\mathrm{T}}\Delta\boldsymbol{\Sigma}, \tag{11}$$

stating that the average of mesoscopic virtual internal work is equal to the macroscopic work done by macroscopic uniform fields $\boldsymbol{E} = \langle\boldsymbol{\varepsilon}\rangle$ and $\boldsymbol{\Sigma} = \langle\boldsymbol{\sigma}\rangle$, where $\langle\cdot\rangle$ stands for volume averaging. In light of the expected nonlinear analysis, we present Eq. (11) and subsequent derivations in an incremental form.

Henceforth, the representative volume element will be thought in terms of a periodic unit cell (PUC) Ω. A natural split of the local displacements $\Delta u_i = \Delta E_{ij}x_j + \Delta u_i^*$ into macroscopic ($\Delta E_{ij}x_j$) and fluctuation (Δu_i^*) parts provides the local strain increment as [40,7]

$$\Delta\boldsymbol{\varepsilon}(\boldsymbol{x}) = \Delta\boldsymbol{E} + \Delta\boldsymbol{\varepsilon}^*(\boldsymbol{x}),\quad \boldsymbol{E} = \langle\boldsymbol{\varepsilon}(\boldsymbol{x})\rangle,\quad \langle\boldsymbol{\varepsilon}^*(\boldsymbol{x})\rangle = \frac{1}{|\Omega|}\int_\Omega \boldsymbol{\varepsilon}^*(\boldsymbol{x})\,\mathrm{d}\Omega = \boldsymbol{0}, \tag{12}$$

where satisfying Eq. $(12)_3$ calls for the periodicity of $\boldsymbol{u}^*$. The constitutive equations of the phases and the corresponding macroscopic relations are then given by

$$\Delta\boldsymbol{\sigma}(\boldsymbol{x}) = L(\boldsymbol{x})(\Delta\boldsymbol{E} + \Delta\boldsymbol{\varepsilon}^*(\boldsymbol{x})),\quad \Delta\boldsymbol{\Sigma} = L^{\mathrm{hom}}\Delta\boldsymbol{E}. \tag{13}$$

Substituting Eqs. $(12)_1$ and $(13)_1$ into Eq. (11) yields

$$\delta\boldsymbol{E}^{\mathrm{T}}\langle L(\boldsymbol{x})(\Delta\boldsymbol{E} + \Delta\boldsymbol{\varepsilon}^*(\boldsymbol{x}))\rangle + \langle\delta\boldsymbol{\varepsilon}^{*\mathrm{T}}(\boldsymbol{x})L(\boldsymbol{x})(\Delta\boldsymbol{E} + \Delta\boldsymbol{\varepsilon}^*(\boldsymbol{x}))\rangle = \delta\boldsymbol{E}^{\mathrm{T}}\Delta\boldsymbol{\Sigma}. \tag{14}$$

Since the variations $\delta\boldsymbol{E}$ and $\delta\boldsymbol{\varepsilon}^*(\boldsymbol{x})$ are independent, the preceding equation can be split into two equalities

$$\delta\boldsymbol{E}^{\mathrm{T}}(\langle L(\boldsymbol{x})\rangle\Delta\boldsymbol{E} + \langle L(\boldsymbol{x})\Delta\boldsymbol{\varepsilon}^*(\boldsymbol{x})\rangle) = \delta\boldsymbol{E}^{\mathrm{T}}\Delta\boldsymbol{\Sigma}, \tag{15}$$
$$\langle\Delta\boldsymbol{\varepsilon}^{*\mathrm{T}}(\boldsymbol{x})L(\boldsymbol{x})\rangle\Delta\boldsymbol{E} + \langle\Delta\boldsymbol{\varepsilon}^{*\mathrm{T}}(\boldsymbol{x})L(\boldsymbol{x})\Delta\boldsymbol{\varepsilon}^*(\boldsymbol{x})\rangle = \boldsymbol{0}.$$

Finally, standard finite element discretization

$$\Delta\boldsymbol{u}^*(\boldsymbol{x}) = \mathbf{N}(\boldsymbol{x})\Delta\boldsymbol{r},\quad \Delta\boldsymbol{\varepsilon}^*(\boldsymbol{x}) = \mathbf{B}(\boldsymbol{x})\Delta\boldsymbol{r}, \tag{16}$$

provides upon introducing Eq. (16) into Eq. (15) the resulting system of algebraic equations in the form

$$\begin{bmatrix} \int_\Omega L(\boldsymbol{x})\,\mathrm{d}\Omega & \int_\Omega L(\boldsymbol{x})\,\mathbf{B}(\boldsymbol{x})\,\mathrm{d}\Omega \\ \int_\Omega \mathbf{B}^{\mathrm{T}}(\boldsymbol{x})L(\boldsymbol{x})\,\mathrm{d}\Omega & \int_\Omega \mathbf{B}^{\mathrm{T}}(\boldsymbol{x})L(\boldsymbol{x})\,\mathbf{B}(\boldsymbol{x})\,\mathrm{d}\Omega \end{bmatrix} \begin{Bmatrix} \Delta\boldsymbol{E} \\ \Delta\boldsymbol{r} \end{Bmatrix} = \begin{Bmatrix} |\Omega|\Delta\boldsymbol{\Sigma} \\ \boldsymbol{0} \end{Bmatrix}, \tag{17}$$

where $\mathbf{N}$ and $\mathbf{B}$ are standard interpolation and strain matrices, respectively, and $\Delta\boldsymbol{r}$ is the increment of nodal fluctuation displacements.

Point out that Eq. (17) represents the most general formulation and allows for three specific loading scenarios:

- Stress-based formulation which assumes that the system is loaded by the prescribed macroscopic stress $\Delta\boldsymbol{\Sigma}$. Such loading conditions might be adopted if the interest is on the effective elastic properties and macroscopic strength only as they do not allow for moving down the descending part of the macroscopic stress–strain curve [20].
- To overpass the preceding obstacle the strain-based formulation might be employed by prescribing the macroscopic strain $\Delta\boldsymbol{E}$. Because $\delta\boldsymbol{E} = \boldsymbol{0}$, Eq. (17) simplifies as

$$\int_\Omega \mathbf{B}^{\mathrm{T}}(\boldsymbol{x})L(\boldsymbol{x})\,\mathbf{B}(\boldsymbol{x})\,\mathrm{d}\Omega\,\Delta\boldsymbol{r} = -\int_\Omega \mathbf{B}^{\mathrm{T}}(\boldsymbol{x})L(\boldsymbol{x})\,\mathrm{d}\Omega\,\Delta\boldsymbol{E}. \tag{18}$$

  On the contrary, this formulation provides no opportunity for generating a one-dimensional macroscopic stress state typical of laboratory conditions [19].
- Combining both approaches opens the way to mixed loading conditions to drive the analysis in the displacement control regime while keeping the one-dimensional format of the macroscopic stress–strain law. For example, for the state of plane stress the one dimensional macroscopic stress–strain curve $\Sigma_{xx}\times E_{xx}$ can be derived by setting $E_{xx} = \overline{E}, \Sigma_{yy} = \Sigma_{xy} = 0$ in Eq. (17).

Both the strain-based formulation and mixed loading/boundary conditions will be examined in the next section. But before proceeding with damage analysis in Section 4 we provide predictions of the effective elastic properties of both types of masonry arrangement, regular and irregular, to appreciate the corresponding degree of anisotropy. Attention is limited to the state of plane stress.

3.1. Macroscopic elastic properties of Placa masonry

The regular periodic unit cell typical of Placa masonry including the geometry and finite element mesh is plotted in Fig. 4. This relatively fine mesh consisting of 60800 quadrilateral elements with a bilinear approximation of the displacement field is also adopted later in nonlinear simulations. The elastic moduli and Poisson ratios of both the brick and mortar are taken from Table 1.

To derive the effective elastic properties, one may use either Eq. (17) or (18) to get the effective compliance and stiffness matrices, respectively. For illustration, the plane stress effective stiffness matrix follows from system (18) by solving three successive elasticity problems. To that end, the periodic unit cell is loaded, in turn, by each component of $\boldsymbol{E}$ ($\boldsymbol{E}^{\mathrm{T}} = \{E_{xx}, E_{yy}, 2E_{xy}\}$), while the other components vanish. The volume stress averages normalized with

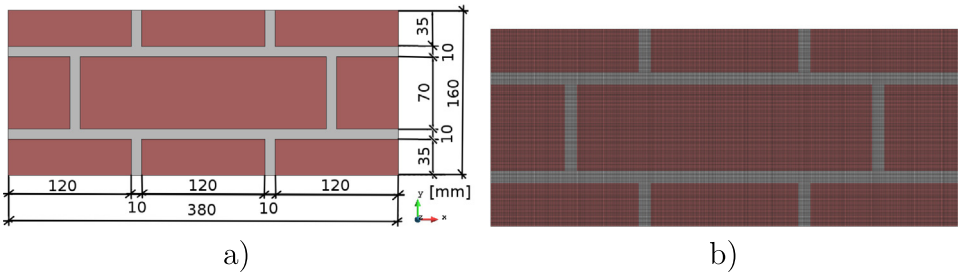

Fig. 4. Periodic unit cell for regular masonry: (a) Geometry, (b) Finite element mesh.

Table 2
Effective elastic properties of Placa masonry.

E_x [GPa]	E_y [GPa]	G_{xy} [GPa]	ν_{xy} [–]	ν_{yx} [–]
6.68	4.03	0.67	0.089	0.047

respect to $\boldsymbol{E}$ then furnish individual columns of $\mathbf{L}^{\text{hom}}$. Similarly, to arrive at the effective compliances matrix $\mathbf{M}^{\text{hom}}$ one exploits Eq. (17) while prescribing the macroscopic stress $\boldsymbol{\Sigma}$.

The results appear in Table 2 clearly identifying the orthotropic material symmetry of the Placa masonry. As for the Poisson ratio ν_{ij}, the notation is taken from [41], i.e., the off-diagonal components of the compliance matrix $\mathbf{M}$ are $M_{12} = -\nu_{xy}/E_y, M_{21} = -\nu_{yx}/E_x$, where E_x, E_y are the Young's moduli in the x and y directions, respectively. The shear modulus G_{xy} follows from $G_{xy} = 1/M_{33}$.

3.2. Macroscopic elastic properties of irregular masonry

As already mentioned in the introductory part, the derivation of statistically equivalent periodic unit cell goes beyond the present scope. The results stored in Table 3 were obtained from simulations carried out for five representative volume elements in Fig. 5. These were constructed from randomly taken photographs of the outer wall of the church in Fig. 2(c). One particular example is seen in Fig. 5(a) for illustration.

All simulations were performed using constant strain triangular elements evident in Fig. 5(b) the number of which being equal to 46000 on average. The elastic material properties of the mortar and sandstone were adopted again from Table 1. The material orthotropy evident from Table 3 complies well with the arrangement of stones in the masonry wall. Although the analyzed masonry could be classified as rubble rather than periodic or quasi-periodic [14,15,42], more or less continuous bed joints could be identified in all samples supporting the resulting material orthotropy.

The differences in the resulting macroscopic moduli and Poisson ratios are merely attributed to mesostructural details of individual RVEs and small differences in the volume fractions of stones available in Table 3. One may also point out the application of periodic homogenization for non-periodic geometries suggesting the homogeneous rather than periodic boundary conditions to adopt for $\boldsymbol{u}^*$. However, discussing the impact of boundary conditions on the resulting predictions is not the objective of this work and the interested reader is referred to [43,44] for additional details on this subject.

Table 3
Effective elastic properties of irregular masonry.

Test window	E_x [GPa]	E_y [GPa]	G_{xy} [GPa]	ν_{xy} [–]	ν_{yx} [–]	Volume fractions stones	Volume fractions mortar
RVE 1	1.980	1.063	0.404	0.078	0.147	0.777	0.223
RVE 2	1.511	0.869	0.367	0.097	0.169	0.770	0.230
RVE 3	1.935	1.259	0.485	0.095	0.144	0.817	0.183
RVE 4	2.142	1.003	0.413	0.083	0.177	0.774	0.226
RVE 5	2.346	1.057	0.432	0.082	0.182	0.802	0.198
Mean	1.983	1.050	0.420	0.087	0.163	0.788	0.212

4. Nonlinear macroscopic stress–strain curves

Apart from effective elastic properties, the nonlinear finite element simulation of masonry structures requires introduction of macroscopic strength and fracture properties depending on the type of macroscopic constitutive law. Given the material orthotropy of masonry walls, the orthotropic damage model described in Section 2 appears as a natural choice. Lacking the fracture properties of both the mortar and bricks/stones in compression, the present section concentrates on the prediction of macroscopic tensile strengths and fracture energies associated with principal material directions. These quantities follow from the macroscopic stress–strain curves.

While extracting the tensile strength is simple, calculating the fracture energy deserves attention. In analogy with the smeared crack model [45], recall also Eq. (5), it was shown in [6] that the fracture energy can be calculated as the area under the stress–strain curve multiplied by the PUC dimension parallel to the loading direction, i.e., $l_{ch} = (L, H)$ where L, H are the horizontal and vertical dimensions of the periodic unit cell, respectively. For mixed formulation considering the loading in the x direction ($E_{xx} = \bar{E}, \Sigma_{yy} = \Sigma_{xy} = 0$), this is evident from

$$U = U^{el} + W_{cr,x} = E_{xx}L, \quad E_{xx} = \frac{\Sigma_{xx}}{E_x^{\text{hom}}} + E_{d,xx}, \quad E_{d,xx} = \frac{W_{cr,x}}{h}, \tag{19}$$

where, in accord with the concept of the first-order homogenization outlined in Section 3, the macroscopic displacement U is assumed linear over the representative volume element. The elastic part of the macroscopic strain E_{xx}^{el} is written in terms of the homogenized Young's modulus E_x^{hom} and the macroscopic stress Σ_{xx}, and the macroscopic damage strain $E_{d,xx}$ is expressed as the macroscopic crack opening $W_{cr,x}$ smeared over a certain distance h. Comparing Eqs. $(19)_1$ and $(19)_3$ readily provides $h = L$ so that

$$\begin{aligned} G_{F,x} = & \int_0^{W_{cr,x}^{max}} \Sigma_{xx}\, \mathrm{d}W_{cr,x} = \int_0^{f_{t,x}} \left(E_{xx} - E_{xx}^{el}\right) L\, \mathrm{d}\Sigma_{xx} = \\ = & \; L \int_0^{E_{xx}^{max}} \Sigma_{xx}(E_{xx})\, \mathrm{d}E_{xx}. \end{aligned} \tag{20}$$

The mixed loading/boundary conditions guarantee that the Σ_{xx} stress component in Eq. (20) is the only non-zero stress component for a given loading direction. An analogous expression is obtained for the loading direction along the y-axis

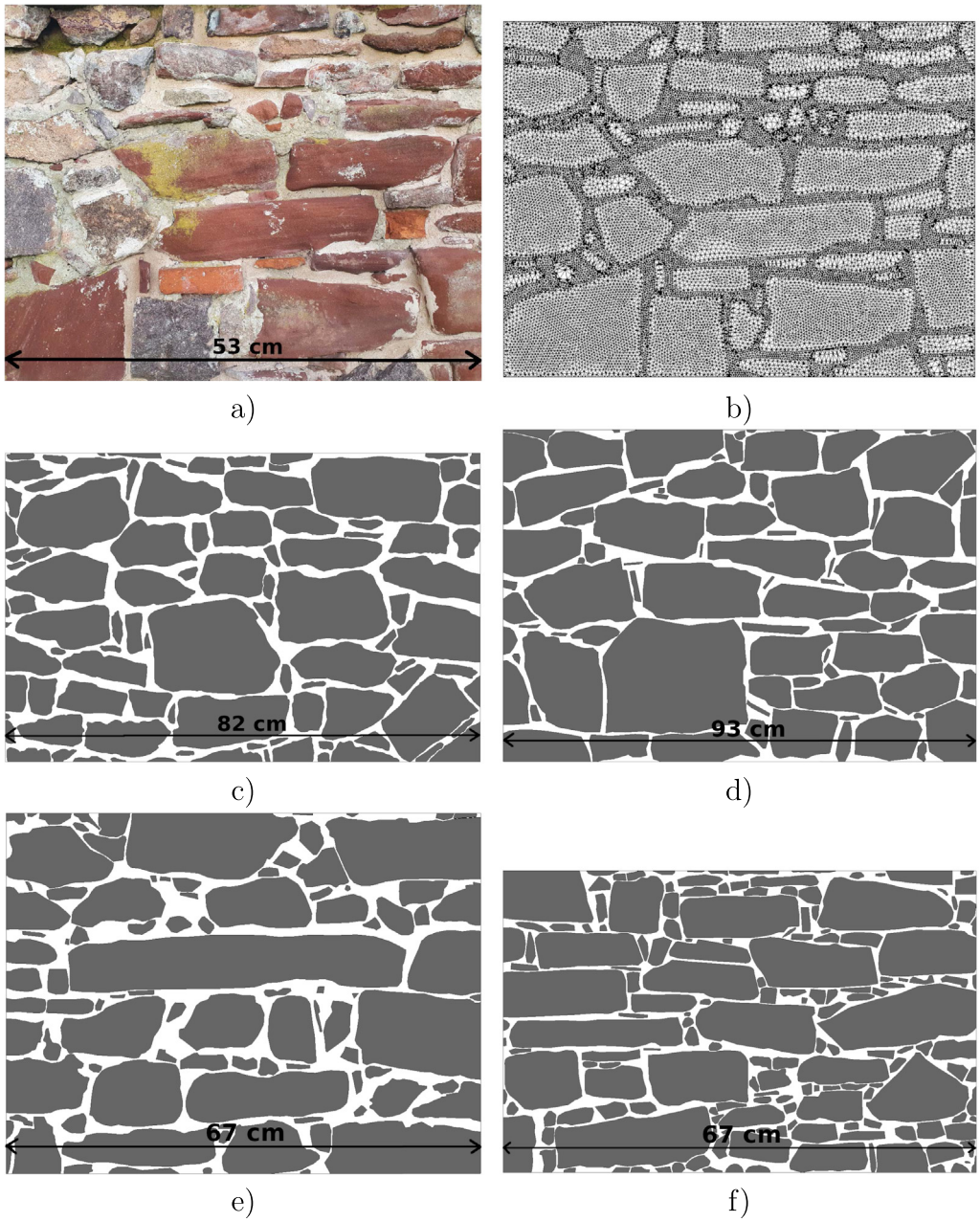

Fig. 5. Examples of irregular masonry test window: (a) RVE 1 geometry, (b) RVE 1 finite element mesh, (c) RVE 2 geometry, (d) RVE 3 geometry, (e) RVE 4 geometry, (f) RVE 5 geometry.

$$G_{F,y} = H \int_0^{E_{yy}^{max}} \Sigma_{yy}(E_{yy})\, \mathrm{d}E_{yy}. \tag{21}$$

It is also worth mentioning, given the first term on the right-hand side of Eq. (20), that G_F in both equations is assumed to be a material property independent of size.

4.1. Placa masonry

The periodic unit cell in Fig. 4 was loaded in tension along the directions x and y of material orthotropy in turn by the prescribed macroscopic strain E_{xx} and E_{yy}, respectively. Based on particular formulation, the case of uniaxial strain, strain-based formulation (strain), or uniaxial stress, stress-based formulation with mixed loading/boundary conditions (mixed), arise.

The macroscopic stress–strain curves plotted in Fig. 6(a) for loading in the x direction clearly identify the differences in the predictions provided by the two constitutive models. For illustration, both the strain-based (strain) and mixed type of loading/boundary conditions (mixed) are examined. The solid lines associate with the orthotropic damage model (ODM). A significantly higher tensile strength is attributed to the property of ODM, which keeps the damage parameter for the direction perpendicular to the loading direction essentially zero so there is no elastic stiffness degradation contrary to the isotropic scalar damage model (SDM), the dashed lines in Fig. 6(a). The evolution of damage parameter for ODM along the loading direction appears more distributed compared to that of SDM, which suggests localization of damage solely into the head joints, Figs. 7(a,b).

The loading direction along the y-axis provides qualitatively different results, which are, however, not surprising given the

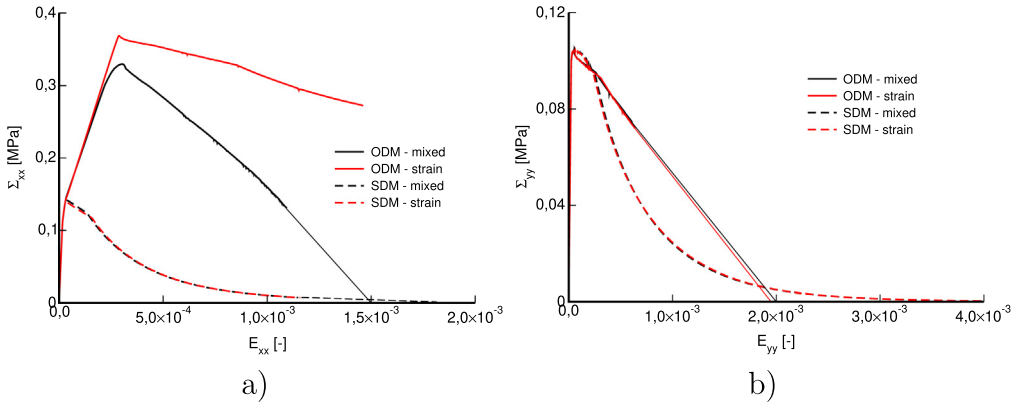

Fig. 6. Macroscopic stress–strain curves for regular (Placa) masonry: (a) Strain E_{xx} applied, (b) Strain E_{yy} applied (ODM - orthotropic damage model, SDM - isotropic scalar damage model).

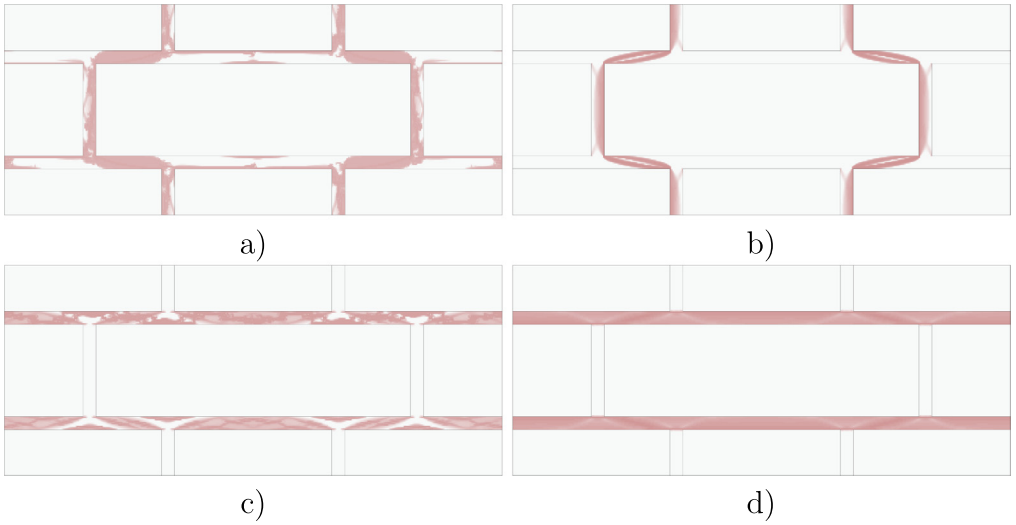

Fig. 7. Evolution of damage parameter for regular (Placa) masonry: (a) ODM, E_{xx}, (b) SDM, E_{xx}, (c) ODM, E_{yy}, (d) SDM, E_{yy}.

geometrical arrangement. Because mortar is much weaker compared to bricks, the bed joint is the weakest link, as evident from Figs. 7(c,d). Thus even with ODM, the non-degrading elastic stiffness along the x-axis provides no support resulting in a similar behavior predicted by both models.

Unlike the macroscopic tensile strength, the evaluation of homogenized fracture energies from the macroscopic stress–strain curves is not that straightforward, given difficulty in converging to the zero macroscopic stress. Therefore, for non-converged simulations the stress–strain curves were ad hoc prolonged as indicated by straight thin lines in Fig. 6. As seen in Fig. 6(a), such a simple remedy was not acceptable for ODM combined with the strain-based formulation. Although not so obvious for other scenarios, the formulation based on the mixed loading/boundary conditions was employed to extract the homogenized fracture properties. The macroscopic strengths and fracture energies derived from Eqs. (20) and (21) are summarized in Table 4.

Table 4
Macroscopic tensile strength and fracture energies from $\Sigma \times E$ diagrams (Placa masonry).

Analysis	$\Sigma_{xx} \times E_{xx}$		$\Sigma_{yy} \times E_{yy}$	
type	$f_{t,x}$ [kPa]	$G_{F,x}$ [N/m]	$f_{t,y}$ [kPa]	$G_{F,y}$ [N/m]
SDM mixed	140.0	20.7	104.0	12.2
SDM strain	142.5	20.8	104.1	12.2
ODM mixed	329.7	107.6	103.5	16.9
ODM strain	368.6	–	103.7	16.5

4.2. Irregular masonry

Five representative volume elements in Fig. 5 were examined to address the influence of constitutive model and formulation of the homogenization problem. The same loading conditions as in the Placa masonry were considered.

The evolution of macroscopic stress Σ as a function of the applied macroscopic strain E is plotted for two selected RVEs in Fig. 8. We first observe that the stone layout favoring weaker "bed" joints results again in lower tensile strengths in the vertical direction, compare Figs. 8(a) and (b). This supports the results obtained already by elastic homogenization in Section 3. It is also seen that both homogenization formulations (strain and mixed) yield almost identical prediction of the macroscopic response.

Contrary to Placa masonry, there is also no difference in the prediction of macroscopic strength provided by the two constitutive models (ODM and SDM). Nevertheless, in the post-peak regime,

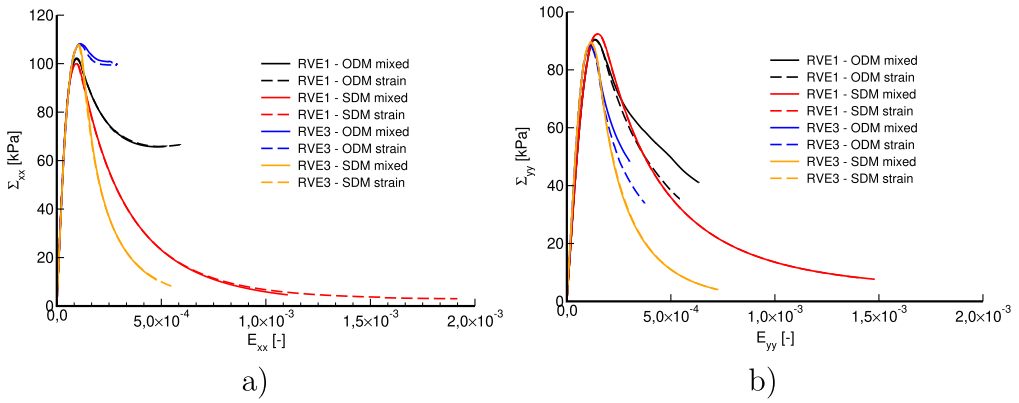

Fig. 8. Macroscopic stress–strain curves for irregular masonry. Testing the influence of microstructure, formulation of homogenization problem, and choice of constitutive model: (a) Strain E_{xx} applied, (b) Strain E_{yy} applied (ODM - orthotropic damage model, SDM - isotropic scalar damage model).

the softening branch cannot be captured well by ODM owing to a stress locking effect which appears for larger values of the damage parameter and the corresponding crack opening [46]. This effect leads to a spurious stress transfer produced by the finite element interpolation. This was documented quite well on a regular masonry when loading the periodic unit cell in Fig. 4 by E_{xx}. We observed a misalignment of principal strain directions with respect to the element edges on the horizontal crack parts. Inevitable rotations of the principal strain directions appear also in the vertical parts where the crack propagation initiates at different layers of the finite element mesh in the mortar phase due to rounding errors. Contrary to that, no such effect was identified for the loading along the y-axis by E_{yy} where the principal strain directions were found well aligned with the element edges for the entire loading process. As suggested in [47], this phenomenon might be suppressed by employing higher-order interpolation elements or by the transition to a scalar damage model for the large crack openings. But this goes beyond the present scope and will be the subject of further investigation. This is also why the scalar isotropic damage model will be employed in all the remaining analyses.

It might be of some interest mentioning the computational burden which was found similar to both damage models and for converged solutions the analysis lasted around 6 h for all RVEs in Fig. 5 using 4× Intel(R) Xeon(R) CPU E5-2630 v3 2.40 GHz with 32 processors and 128 GB RAM.

4.2.1. Fracture energy from wedge splitting test

Because lacking sufficient support for applying a periodic homogenization in the absence of statistically equivalent periodic unit cell, recall randomly chosen non-periodic mesostructures in Fig. 5, we estimate the fracture energy from a numerical representation of a wedge splitting test, see Fig. 9(a), one would perform in laboratory [48]. Two laboratory specimens being represented by RVE 1 and RVE 3 are considered allowing us to partially address the influence of both the specimen size and mesostructural details. We proceed in the footsteps of [49] and define four wedge scenarios as depicted in Figs. 9(c,d).

To begin with, we recall Eq. (20) and write the fracture energy G_F as

$$G_F = \int_0^{w_{cr}^{max}} \sigma(w)\,\mathrm{d}w = l_{ch}\int_0^{\varepsilon_d^{max}} \sigma(w)\,\mathrm{d}\varepsilon = \frac{-\Delta E_{int}}{B\Delta l_{cr}}, \tag{22}$$

where $l_{ch} = w/\varepsilon_d$ now represents the localization band, B is the specimen thickness and $(-\Delta E_{int})$ is the loss of internal energy due crack advance Δl_{cr}. Following RILEM [50], we may now derive the average fracture energy G_f by integrating Eq. (22) as

$$\int \mathrm{d}E_{int} + G_f B \int \mathrm{d}l_{cr} = 0, \tag{23}$$

where G_f is assumed constant given by

$$G_f = \frac{-E_{int}}{A_{cr}} = \frac{1}{A_{cr}}\int_0^{COD^{max}} F(u)\mathrm{d}u, \tag{24}$$

where $A_{cr} = BL_{cr}$ is the fracture surface, L_{cr} is the total length of traction free surfaces, and COD_{max} represents the maximum crack opening displacement COD attained at complete separation.

To obtain the force displacement curve $F \times COD$, the test simulation was carried out in the displacement control regime by prescribing $COD = 2u$, where u is the horizontal displacement specified at two points indicated by the reaction force F in Fig. 9(a).

An example of the reaction force - displacement curve $F \times u$ for the smallest notch size $a = H/6$ is plotted in Fig. 9(b) to confirm the symmetry of the analysis. To understand the difference in the shape of the two curves, we should point out the different size of RVE 1 and RVE 3 as well as significant differences in the local arrangement of stones. The corresponding $F \times COD$ curves for the assumed notch to depth ratios $a/H = 1/6, 1/3, 1/2, 2/3$ are shown in Figs. 9(e,f). The selected damage patterns, compatible with mesoscopic details, are seen in Fig. 10.

The resulting fracture energies $G_{f,x}$ derived from Eq. (24) are stored in Table 5. The fracture surface A_{cr} was estimated from the plots of final damage pattern by setting L_{cr} the sum of all segments for which $\omega = 1$. The last column in Table 5 shows for illustration the fracture energy $G^*_{f,x}$ obtained by assuming the fracture surface $A_{cr} = (H - a)B$ generally adopted for quasi-homogeneous and isotropic materials such as concrete or mortar.

For such materials, it has been shown in [51] that G_f is a function of notch size and rapidly decreases to zero as $a \to H$ as seen in Fig. 11(a) showing also the proposed bilinear form of the local fracture energy g_f to estimate G_F. Contrary to that, the masonry material does not show such a strong notch size dependence. This is evident from the plot of fracture energy $G_{f,x}$ as a function of the notch size a in Fig. 11(b).

In fact, the damage in masonry localizes into the mortar joints representing more or less a constant localization band, which does not disappear even when approaching a free boundary. Thus the fracture energy G_F derived from Eq. (22) is indeed a constant independent of the extent of damage and consequently $G_f \approx G_F$ providing the fracture surface $A_{cr} = BL_{cr}$. Inadequacy of considering the fracture surface A_{cr} be proportional to the un-notched ligament size $H - a$ for highly heterogeneous materials is also evident from Fig. 11(b).

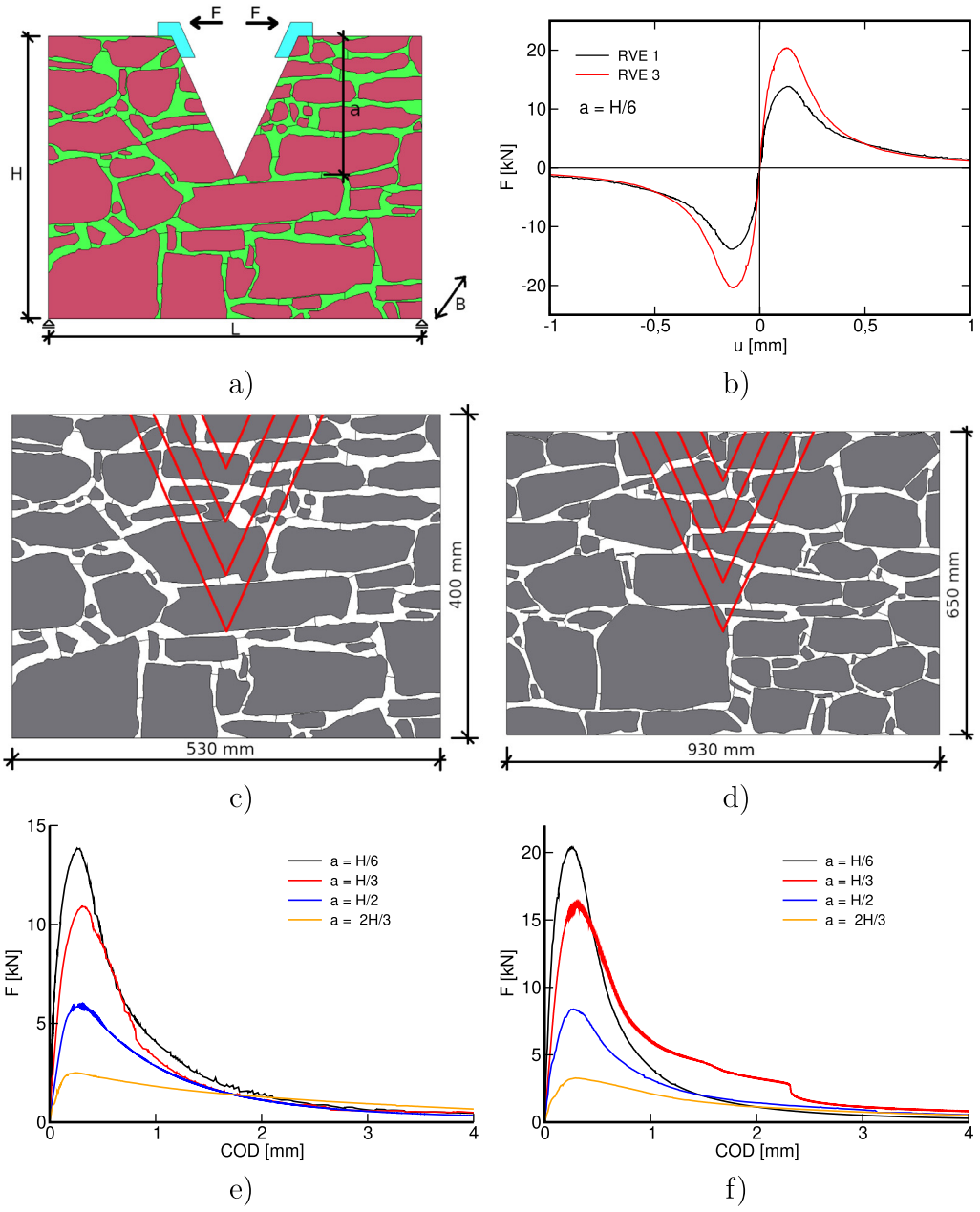

Fig. 9. Wedge splitting test: (a) general scheme, (b) example of $F \times COD$ curve for $a = 1/6H$, (c) wedge geometry - RVE 1, (d) wedge geometry - RVE 3. Evolution of the reaction force F as a function of the applied COD: (e) RVE 1, f) RVE 3.

4.2.2. Fracture energy from homogenization

Having at hand an estimate of fracture energy from the wedge splitting test being around 22 N/m we return back to Eq. (20) to compare this value with the one predicted by homogenization. The need for a sufficiently large RVE is addressed first by examining three medium-size RVEs randomly extracted from RVE 3. These are denoted as M1, M2, and M3 in Fig. 12(a). To keep the uniaxial stress state, the mixed formulation is employed to acquire the macroscopic tensile stress–strain data.

This first experiment considers tension along the x-axis by prescribing the macroscopic strain E_{xx} while maintaining $\Sigma_{yy} = \Sigma_{xy} = 0$. The resulting macroscopic stress–strain curves appear in Fig. 12(b). Although the volume fraction of stones c_s listed in Table 6 does not very much and is quite close to that of the large RVE 3 for which $c_s = 0.817$, recall Table 3, the macroscopic response is quite different. This is in agreement with the final damage pattern plotted for individual RVEs in Figs. 12(c-e). Clearly, the arrangement of stones in samples M1 and M3 can hardly be considered as periodic and thus representative of the large domain of masonry. In this regard, the sample M2 only could be deemed satisfactory resulting in fracture energy $G_{F,x} = 20.2$ N/m[1], the only value in Table 6 comparable with the average value $\overline{G}_{f,x} = 21.7$ N/m provided by the wedge splitting test. However, in terms of the effective elastic properties, even the M2 sample does not contain sufficient morphological details implying a considerably stiffer elastic response compared to that provided

[1] Note that in order to calculate the fracture energy, the stress–strain diagrams in Fig. 12(b) were artificially prolonged and truncated at the maximum strain $E_{xx} = 0.002$.

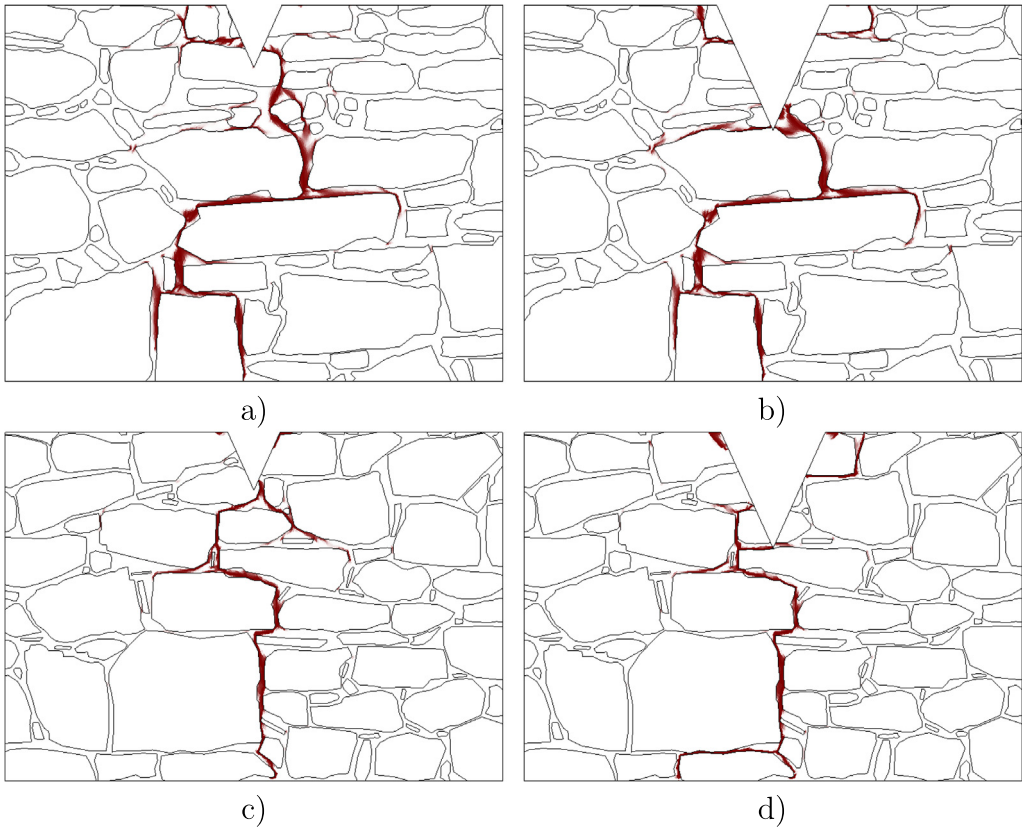

Fig. 10. Wedge splitting test - evolution of damage parameter ω: (a) RVE 1 $a = 1/6H$, (b) RVE 1 $a = 1/3H$, (c) RVE 3 $a = 1/6H$, (d) RVE 3 $a = 1/3H$.

Table 5
Fracture energy from wedge splitting test ($B = 1$m).

Test window	a [m]	L_{cr} [m]	$\int F\,du$ [Nm]	$G_{f,x}$ [N/m]	$G^*_{f,x}$ [N/m]
RVE 1	0.67	0.750	14.47	**24.5**	43.6
	0.133	0.745	11.75	**19.9**	44.0
	0.200	0.380	7.95	**20.9**	39.8
	0.267	0.320	7.38	**21.7**	55.5
RVE 3	0.108	0.694	15.56	**22.4**	28.7
	0.217	1.005	20.40	**20.3**	47.1
	0.325	0.502	11.68	**23.3**	35.9
	0.433	0.378	7.68	**20.3**	35.4

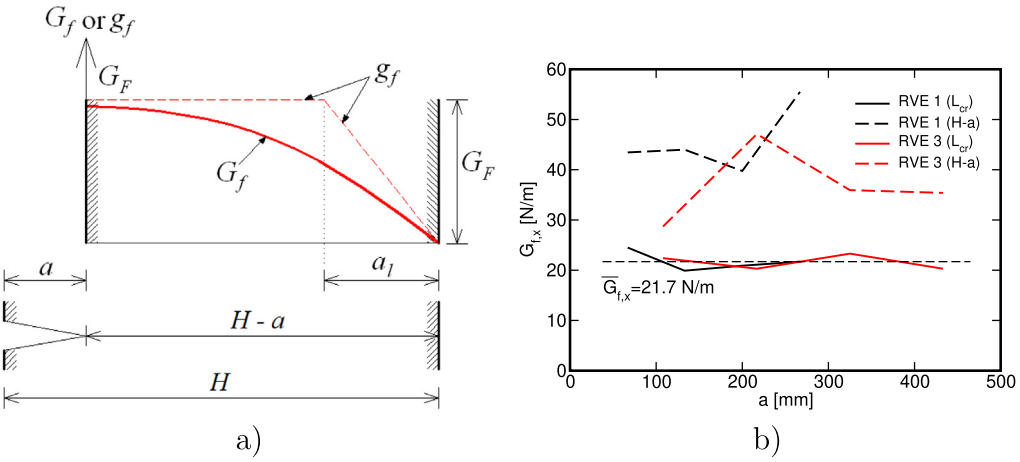

Fig. 11. Estimate of size-independent fracture energy $G_{F,x}$: (a) Bilinear form of local fracture energy g_f proposed in [51], (b) $G_{f,x}$ from Eq. (24) plotted as a function of a.

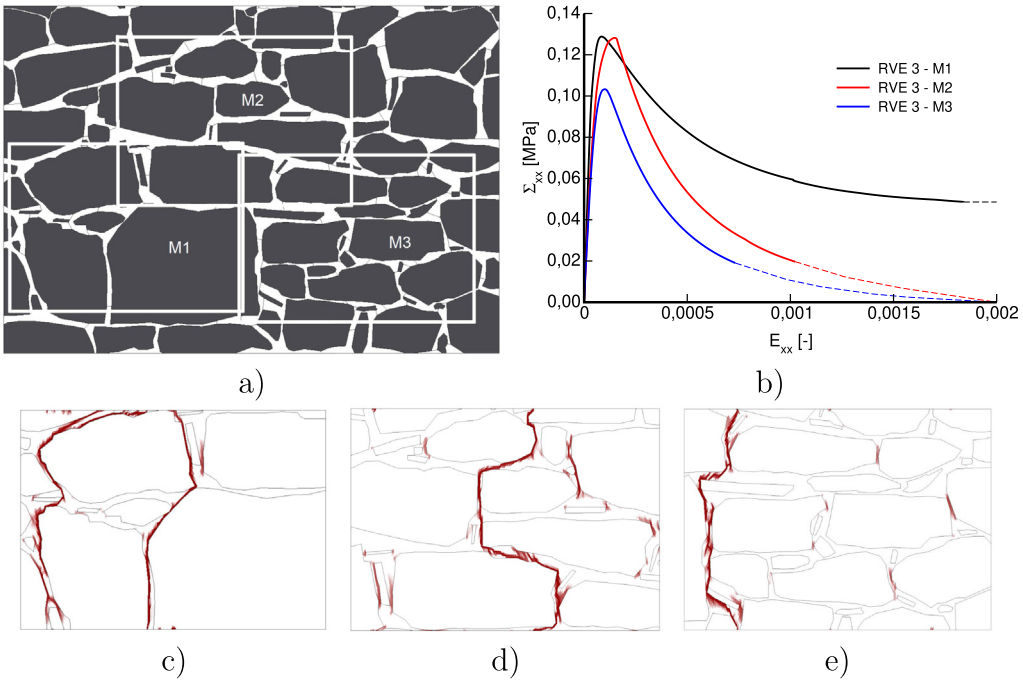

Fig. 12. (a) Medium size RVEs M1, M2, M3, (b) Macroscopic stress–strain curves, (c)-(e) Damage patterns: (c) M1, (d) M2, (e) M3.

Table 6
Fracture energy from homogenization. Test windows ($L = 292$ mm, $H = 315$ mm, $B = 1$ m) extracted from RVE 3.

Test window	c_s [–]	E_x [GPa]	E_y [GPa]	L [m]	$\int \Sigma_{xx}\, dE_{xx}$ [N/m^2]	$G_{F,x}$ [N/m]
M1	0.844	2.87	2.22	0.292	137.6	40.2
M2	0.845	3.87	1.96	0.292	69.4	**20.2**
M3	0.810	2.47	1.74	0.292	46.2	13.7

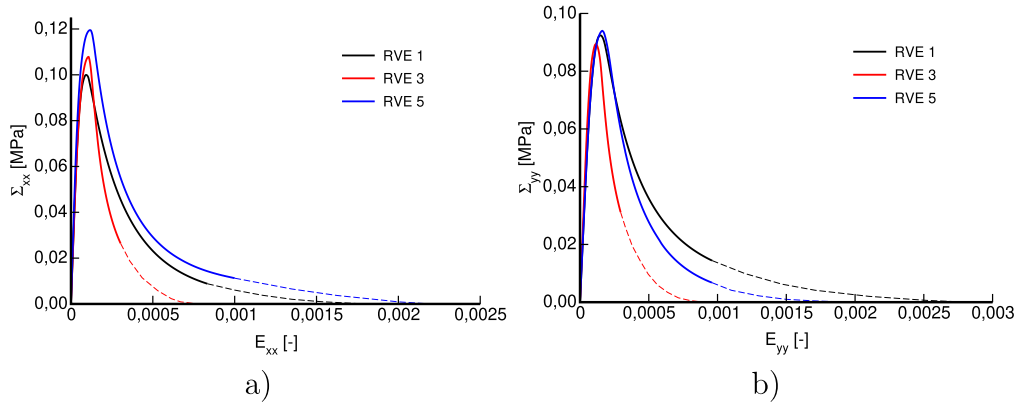

Fig. 13. Macroscopic stress–strain curves for irregular masonry with artificially prolonged softening part to attain zero macroscopic stress at complete failure: (a) Strain E_{xx} applied, (b) Strain E_{yy} applied.

by RVE 3, compare the effective elastic moduli E_x, E_y in Tables 3 and 6, respectively.

In the light of these findings, we turn our attention back to large RVEs in Fig. 5. Because representing sufficient diversibility in mesostructural details, we accord our attention to RVE 1, RVE3, and RVE 5 only. The macroscopic stress–strain curves for the two loading directions (tension along x and y axes) are displayed in Fig. 13. To obtain the macroscopic fracture energies given by Eqs. (20) and (21), the non-converged solutions were again artificially prolonged as indicated by the dashed lines.

The macroscopic fracture properties are stored in Tables 7 and 8. We observe some differences in the predicted values of the macroscopic tensile strength. It is believed that this, together with initial nonlinearity before tensile softening, is caused by the evolution of isolated damage zones due to local tension, which in turn depends on specific mesoscopic morphology of individual RVEs. The material heterogeneity producing local stress concentrations is an elementary argument to support a relatively low macroscopic tensile strength not even exceeding the strength of the mortar phase, particularly in the y direction normal to the

Table 7
Fracture energies from $\Sigma \times E$ diagrams.

Test	L	H	$\int \Sigma_{xx} E_{xx}$	$\int \Sigma_{yy} E_{yy}$	$G_{F,x}$	$G_{F,y}$
window	[m]		[Pa]		[N/m]	
RVE 1	0.53	0.40	35.6	49.2	18.9	19.7
RVE 3	0.93	0.65	22.9	22.2	21.3	14.4
RVE 5	0.67	0.51	48.0	37.0	32.2	16.4

Table 8
Macroscopic tensile strength and critical crack opening displacement.

Test	$f_{t,x}$	$f_{t,y}$	$W_{cr,x}^{max}$	$W_{cr,y}^{max}$	$W_{cr,x}^{max,*}$	$W_{cr,y}^{max,*}$	$W_{cr0,x}$	$W_{cr0,y}$
window	[kPa]		[mm]		[mm]		[mm]	
RVE 1	99.9	92.4	0.95	1.13	0.38	0.43	0.19	0.21
RVE 3	107.8	89.4	0.71	0.59	0.40	0.32	0.20	0.16
RVE 5	119.5	94.0	1.47	1.02	0.54	0.35	0.27	0.17

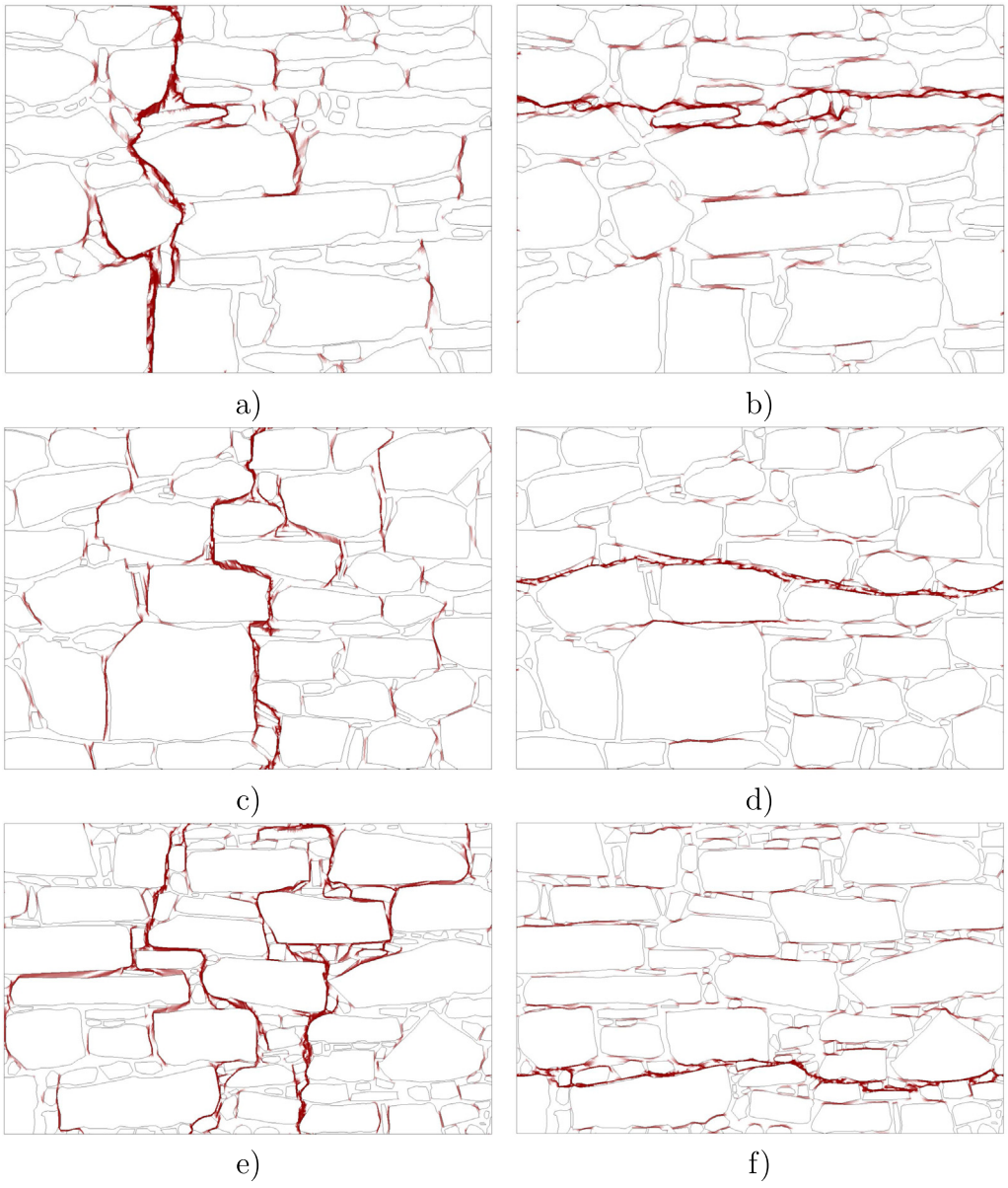

Fig. 14. Evolution of damage parameter ω for irregular masonry: (a) RVE 1, E_{xx}, (b) RVE 1, E_{yy}, (c) RVE 3, E_{xx}, (d) RVE 3, E_{yy}, (e) RVE 5, E_{xx}, (f) RVE 5, E_{yy}.

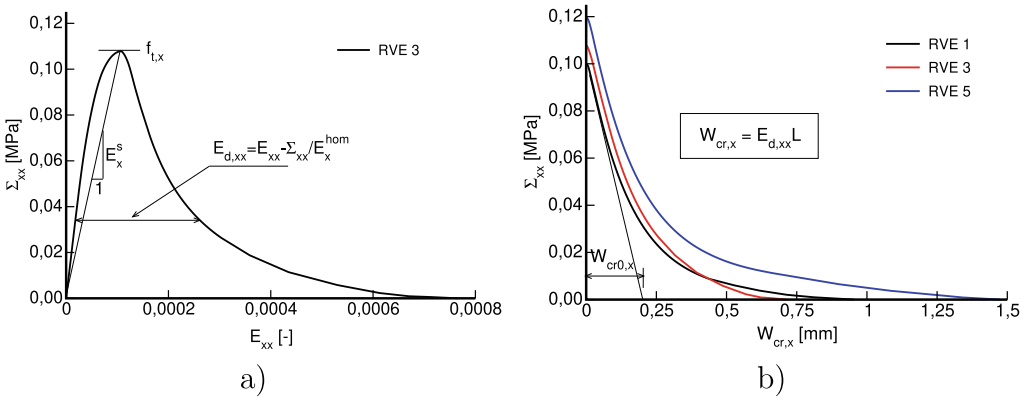

Fig. 15. (a) Example of macroscopic stress–strain diagram $\Sigma_{xx} \times E_{xx}$ for RVE 3, (b) $\Sigma_{xx} \times W_{cr,x}$ diagrams.

Table 9
Fracture energies from $\Sigma \times E$ and $\Sigma \times W_{cr}$ diagrams.

Test	E_x	E_x^s	$G_{F,x}$	$G_{F,x}^*$
window	[GPa]		[N/m]	
RVE 1	1.98	1.08	18.9	17.9
RVE 3	1.94	1.01	21.3	19.3
RVE 5	2.36	1.03	32.2	30.1

"bed" joints. It is clear that the effect of local morphology must also reflect in the prediction of tensile softening and consequently the macroscopic fracture energy. This is evident in the examples of damage pattern in Fig. 14 associated with the last converged step. While the macroscopic stress–strain curves depend on the size of the representative volume element, the corresponding fracture energies are assumed to be a material property. This statement is supported by consistency of the predicted values seen in Table 7.

For the results to be potentially applicable with a commercial software such as ABAQUS we also present in Table 8 estimates of the critical crack opening. While the values of $W_{cr,i}^{max}$ were found from Eq. $(19)_3$ with $h = L, H$ for given values of $E_{d,ii}^{max} = E_{ii}^{max}$ extracted from Fig. 13, the values of $W_{cr,i}^{max,*} = 2G_{f,i}/f_{t,i}$ correspond to the assumption of a linear softening law. Note, however, that none of these values are directly applicable with the adopted exponential softening law where the value of $W_{cr0,i} = G_{f,i}/f_{t,i}$ is needed instead.

To check validity of Eq. (20) one may attempt to estimate the fracture energy G_F directly from the first term on the right-hand side of this equation. The point of departure is Eq. $(19)_2$. Because of nonlinear response prior to exceeding the macroscopic tensile strength f_t, we accepted some simplification by replacing the effective Young modulus E^{hom} in this equation by the secant modulus E^s displayed in Fig. 15(a), see also Table 9 to compare this value with the homogenized elastic modulus taken from Table 3. Exploiting Eq. $(19)_3$ we then arrive at $\Sigma \times W_{cr}$ diagrams in Fig. 15(b) allowing us to calculate the fracture energies G_F^* (the lower bound estimate) as the area under individual diagrams. The results are stored in Table 9 together with the fracture energy derived from the application of $\Sigma \times E$ diagrams in Fig. 13, recall Table 7. Both values are reasonably close up to the error in G_F^* caused by omitting the part of energy associated with the evolution of isolated cracks prior to the onset of softening.

5. Conclusions

The forgoing discussion was intended to review some of the basic aspects of first-order homogenization when applied to quasi-brittle materials. In expectation for solving complex masonry structures we gave up the idea of a fully coupled multiscale analysis and focused on the derivation of basic fracture properties such as strength and fracture energies from computational homogenization considering suitable representative elements. These properties are expected to enter a suitable macroscopic constitutive model exploited in an independent analysis at structural level. In this regard, a simple isotropic scalar damage model and a more advanced anisotropic (orthotropic) damage model were examined and compared. This is also why we limited our attention to pure tensile cracking with no attempt to describe evolution of plastic strains due to, e.g., sliding or triaxial crushing, which in turn would call for a considerably more advanced constitutive model.

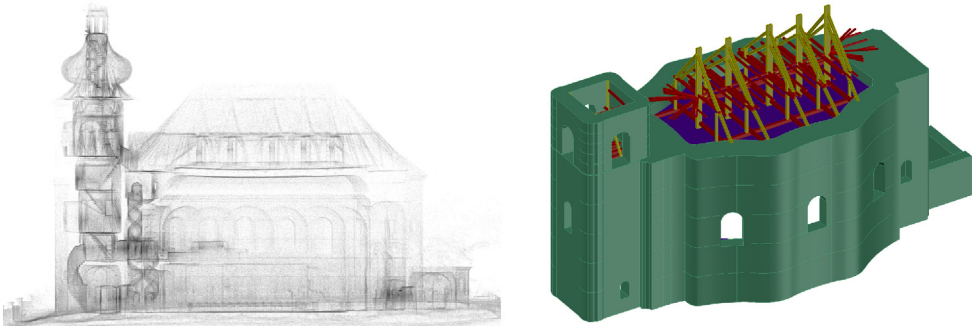

Fig. 16. From laser scanning photogrammetry to 3D model.

The principal findings are:

- Although not considerably different in providing the macroscopic response, the mixed type formulation is preferred to the strain-based formulation allowing us to comply with the uniaxial state of stress.
- Application of the orthotropic damage models appears inappropriate in the solution of the homogenization problem. Contrary to that, a simple isotropic damage model is found to provide meaningful results supported by comparing the results of wedge splitting test and homogenization for irregular masonry. It is reasonable to assume that a similar outcome would be obtained for a regular masonry.
- Owing to a relatively weak anisotropy of historical masonry, the present results also confirm applicability of the isotropic damage model even on macroscale by using some average fracture properties, e.g., $G_F = \sqrt{G_{F,x}G_{F,y}}$. This opens the way to application of various commercial codes such as ABAQUS by employing constitutive models typically formulated for quasi-isotropic materials such as concrete. Nevertheless, application of the modified orthotropic model on macroscale is currently under investigation with reference to a group of historical churches in Broumov region in the Czech Republic. To this end, the homogenized values in Table 3 will also be exploited. Apart from constitutive modeling, attention is accorded to a detailed representation of geometry employing laser scanning and aerial "drone" photogrammetry. An example of a colored point cloud representation of the church in Fig. 2 transformed into a three-dimensional model suitable for meshing and finite element analysis is available in Fig. 16.

Declaration of Competing Interest

The authors declare that they have no known competing financial interests or personal relationships that could have appeared to influence the work reported in this paper.

Acknowledgment

We are thankful for financial support provided by the Czech Science Foundation, project No. 18-24867S.

References

[1] Massart TJ. Multi-scale modeling of damage in masonry structures Ph.D. thesis. Technische Universiteit Eindhoven; 2003.
[2] Petracca M. Computational multiscale analysis of masonry structures Ph.D. thesis. Barcelona, Spain: Technical University of Catalonia; 2016.
[3] de Bellis M, Addessi D. A cosserat-based multi-scale model for masonry structures. Int J Multiscale Comput Eng 2011;9:543–63.
[4] Addessi D, Sacco A. A multi-scale enriched model for the analysis of masonry panels. Int J Solids Struct 2012;49:865–80.
[5] Massart T, Bouillard P, Geers M, Peerlings R. Anisotropic damage effects in masonry walls. J Phys IV 2003;105:149–56.
[6] Zeman J, Šejnoha M. From random microstructures to representative volume elements. Modell Simul Mater Sci Eng 2007;15(4):S325–35.
[7] Šejnoha M, Zeman J. Micromechanics in Practice. Southampton, Boston: WIT Press; 2013.
[8] Milani G, Lourenco P. A simplified homogenized limit analysis model for randomly assembled blocks out-of-plane loaded. Comput Struct 2010;88:690–717.
[9] Milani G, Lourenco P. Monte Carlo homogenized limit analysis model for randomly assembled blocks in-plane loaded. Comput Mech 2010;46(6):827–49.
[10] Cundari G, Milani G. Homogenized and heterogeneous limit analysis model for pushover analysis of ancient masonry walls with irregular texture. Int J Architect Heritage: Conserv, Anal, Restor 2013;7:303–38.
[11] Bertolesi E, Milani G. Quasi-analytical homogenization approach for the non-linear analysis of in-plane loaded masonry panels. Constr Build Mater 2017;146:723–43.
[12] Cavalagli N, Cluni F, Gusella V. Failure surface of quasi-periodic masonry by means of statistically equivalent periodic unit cell approach. Meccanica 2018;53(7):1719–36.
[13] Cavalagli N, Cluni F, Gusella V. Strength domain of non-periodic masonry by homogenization in generalized plane state. Eur J Mech 2018;30(2):113–26.
[14] Tiberti S, Milani G. 2d pixel homogenized limit analysis of non-periodic masonry walls. Comput Struct 2019;219:16–57.
[15] Tiberti S, Milani G. 3d voxel homogenized limit analysis of single-leaf non-periodic masonry. Comput Struct 2020;229:106186.
[16] Tiberti S, Milani G. 3D homogenized limit analysis of non-periodic multi-leaf masonry walls. Comput Struct 2020;234:106253.
[17] D'Altri A, Sarhosis V, Milani G, Rots J, Cattari S, Lagomarsino S, Sacco E, Tralli A, Castellazzi G, de Miranda S. Modeling strategies for the computational analysis of unreinforced masonry structures: Review and classification. Arch Comput Methods Eng 2020;27(4):1153–85.
[18] Papa E, Taliercio A. Anisotropic damage model for the multiaxial static and fatigue behaviour of plain concrete. Eng Fract Mech.
[19] Bernardo V, Krejčí T, Koudelka T, Šejnoha M. Homogenization of unreinforced old masonry wall. Comparison of scalar isotropic and orthotropic damage models. Acta Polytech, CTU Proc 2020;26:1–6.
[20] Krejčí T, Koudelka T, Bernardo V, Šejnoha M. Macroscopic response of regular masonry from homogenization: comparison of isotropic and orthotropic damage models. In: MATEC Web of Conferences, Vol. 310; 2020, p. 8.
[21] Monteiro M, Bento R. Characterization of "placa" buildings, ICIST DTC, Portugal.
[22] Tiago F, Milosevic J, Bento R. Seismic vulnerability assessment of a mixed masonry RC building aggregate by linear and nonlinear analyses. Bull Earthq Eng 2016;14:1765–2327.
[23] D'Altri A, De Miranda S, Castellazzi G, Sarhosis V, Hudson J, Theodossopoulos D. Historic barrel vaults undergoing differential settlements. Int J Architect Heritage 2020;14(8):1196–209.
[24] Zeman J, Šejnoha M. Numerical evaluation of effective properties of graphite fiber tow impregnated by polymer matrix. J Mech Phys Solids 2001;49(1):69–90.
[25] Cavalagli N, Cluni F, Gusella V. Evaluation of a statistically equivalent periodic unit cell for a quasi-periodic masonry. Int J Solids Struct 2013;50(25–26):4226–40.
[26] Grassl P, Xenos D, Nyström U, Rempling R, Gylltoft K. CDPM2: A damage-plasticity approach to modelling the failure of concrete. Int J Solids Struct 2013;50:3805–16.
[27] Koudelka T, Kruis J. Damage-plasticity model of the host rock in a nuclear waste repository. In: AIP Conf Proc.
[28] Bažant ZP, Oh BH. Crack band theory for fracture of concrete. Matériaux et Constr 1983;16(3):155–77.
[29] Krejčí T, Koudelka T, Kruis J. Modeling of building constructions in SIFEL environment. Czech Technical University in Prague; 2011. p. 87. , http://ksm.fsv.cvut.cz/~sifel.
[30] Mazars J. A description of micro and macroscale damage of concrete structures. Int J Fract 1986;25:729–37.
[31] Krejčí T, Koudelka T, Šejnoha J, Zeman J. Computer simulation of concrete structures subject to cyclic temperature loading. In: Topping BHV, Costa Neves LF, Barros RC, editors. Proceedings of the Twelfth International Conference on Civil, Structural and Environmental Engineering Computing. Stirlingshire, United Kingdom: Civil-Comp Press; 2009. paper 131.
[32] Koudelka T, Krejčí T, Šejnoha J. Analysis of a nuclear power plant containment. In: Topping BHV, Costa Neves LF, Barros RC, editors. Proceedings of the Twelfth International Conference on Civil, Structural and Environmental Engineering Computing. Stirlingshire, United Kingdom: Civil-Comp Press; 2009. paper 132.
[33] Marques AI, Candeias PX, Veiga MR, Ferreira JG. Axial compression and bending tests on old masonry walls. In: 3rd International Conference on Protection of historical constructions.
[34] Marques AI, Candeias PX, Ferreira JG, Veiga MR. Ensaios de compressao diagonal em paredes antigas de alvenaria de tijolo. In: CONSTRUCAO 2018, Porto; 2018.
[35] Marques AI, Candeias PX, Ferreira JG, Veiga MR. Caraterizacao de paredes resistentes de alvenaria antiga. In: REHABEND 2016, Spain; 2016.
[36] Kuklik P, Valek M, Gajjar P, Scacco G. The basic tasks in evaluation of ancient structures sustainability and in estimation of enclosure walls bearing capacity. Int J Struct Civil Eng Res 2019;8(4):290–3.
[37] Lourenco P. Strucural masonry analysis: recent developments and prospects. In: 14th International brick and block masonry conference, Sydney; 2008.
[38] Scacco J. Nonlinear numerical evaluation of the bearing capacity and the structure stability of the St. Jacob Church from the Group of Churches, Diploma thesis, Czech Technical University in Prague, Faculty of Civil Engineering; 2018.
[39] Hill R. Elastic properties of reinforced solids - Some theoretical principles. J Mech Phys Solids 1963;11:357–72.
[40] Michel JC, Moulinec H, Suquet P. Effective properties of composite materials with periodic microstructure: A computational approach. Comput Methods Appl Mech Eng 1999;172:109–43.
[41] Bittnar Z, Šejnoha J. Numerical methods in structural engineering. ASCE Press; 1996.
[42] Tiberti S. In- and Out-of-Plane Homogenized Limit Analysis of Non-Periodic Masonry Walls Based on a Novel Pixel/Voxel Strategy, Ph.D. thesis, Politechnico di Milano, Department of Architecture, Build Environment and Cnstruction Engineering; 2020.

[43] Gajdošík J, Zeman J, Šejnoha M. Qualitative analysis of fiber composite microstructure: Influence of boundary conditions. Probab Eng Mech 2006;21:317–29.
[44] Pahr DH, Zusset PK. Influence of boundary conditions on computed apparent elastic properties of cancellous bone. Biomech Model Mechanobiol 2008;7 (6):463–76.
[45] Hillerborg A, Modeer M, Petersson P. Analysis of crack formation and crack growth in concrete by means of fracture mechanics and finite elements. Cem Concr Res 1976;6(6):773–91.
[46] Jirásek M, Zimmermann T. Analysis of rotating crack model. J Eng Mech 1998;124:842–51.
[47] Jirásek M, Zimmermann T. Rotating crack model with transition to scalar damage. J Eng Mech 1998;124:277–84.
[48] Brühwiler E, Wittmann F. The wedge splitting test, a new method of performing stable fracture mechanics tests. Eng Fract Mech 1990;35(1–3):117–25.
[49] Šejnoha J, Šejnoha M, Zeman J, Sýkora J, Vorel J. Mesoscopic study on historic masonry. Struct Eng Mech 2008;30(1):99–117.
[50] RILEM Committee FMC 50. Determination of the fracture energy of mortar and concrete by means of three-point bend tests on notched beams. Mater Struct 1985;18(4):287–90.
[51] Duan K, Hu X, Wittmann F. Thickness effect on fracture energy of cementitious materials. Cem Concr Res 2003;33(4):449–507.